Journal of Alloys and Compounds 501 (2010) 291–296

Contents lists available at ScienceDirect

Journal of Alloys and Compounds

journal homepage: www.elsevier.com/locate/jallcom

# Effect of cooling conditions during casting on fraction of β-$Mg_{17}Al_{12}$ in Mg–9Al–1Zn cast alloy

Tianping Zhu [a,*], Zhan W. Chen [b], Wei Gao [a]

[a] Department of Chemical & Materials Engineering, University of Auckland, New Zealand
[b] Department of Mechanical & Manufacturing Engineering, AUT University, New Zealand

ARTICLE INFO

*Article history:*
Received 30 November 2009
Received in revised form 14 April 2010
Accepted 14 April 2010
Available online 22 April 2010

*Keywords:*
Divorced eutectic
Discontinuously precipitation
EBSD and image analysis

ABSTRACT

The major second phase (β-$Mg_{12}Al_{17}$) that is present in the most commonly used cast magnesium alloy, AZ91, has a strong effect on various properties of the alloy. Thus how casting conditions affect the amount of this phase formed needs to be studied. In the present study, casting of AZ91 was conducted allowing various cooling conditions by employing a chill. Total fraction of β-phase ($f_\beta$), the fraction of the eutectic β phase ($f_{\beta\text{-}eut}$) formed during eutectic solidification, and the fraction of discontinuous β precipitates ($f_{\beta\text{-}d}$) formed during subsequent solid state cooling were quantitatively measured, respectively. It was found that $f_\beta$ was not significantly affected by the variation of cooling history in different locations of the casting. However, $f_{\beta\text{-}eut}$ and $f_{\beta\text{-}d}$ are strongly location-dependent, decreasing and increasing, respectively, towards the chill end of the casting. Explanation on this is given taking into accounts the effects of casting/thermal conditions on solidification and subsequent discontinuous precipitation.



## 1. Introduction

The usage of cast magnesium alloys continues to increase due to the demand for weight reduction and fuel efficiency in the automotive and aerospace industries. Mg–Al alloys are processed using various casting techniques with AZ91 being the most commonly used magnesium alloy for casting. Like many cast alloy systems, Mg–Al alloys solidify into a basic microstructure comprising primary α(Mg) dendrites and eutectic. The eutectic, α(Mg) + β($Mg_{12}Al_{17}$), in Mg–Al alloys is however a divorced one. High cooling rates during high pressure die casting (HPDC) resulted in a fully divorced eutectic where the eutectic (α and β) phases solidify completely separately [1]. In contrast, a partially divorced eutectic morphology is characterized by "islands" of α phase inside eutectic β ($\beta_{\text{-eut}}$) particle [2]. Also, the morphology of eutectic in Mg–Al cast alloys is significantly affected by the Al content in the alloys [3].

Intermetallic β phase is brittle and the mechanical properties of Mg–Al castings are adversely affected by its presence although this is unavoidable [4–8]. The elongation at fracture ($e_f$) and ultimate tensile strength (UTS) are significantly affected by the amount and distribution of the β phase. A low fraction and a fine distribution of the β phase help to withstand a large deformation before fracture. Results reported by Cao and Wessén [9] indicated that $e_f$ and UTS values both decreased with an increasing amount of β phase for a series of Mg–Al cast alloys containing various Al contents. It has also been reported that $e_f$ and UTS values increased once the β phase in AZ91 cast alloy dissolved through solid solution treatment [4]. The fraction of β phase ($f_\beta$) is thus a determining factor for the mechanical properties of AZ91 cast alloy.

The effects of solidification rate on microstructural features such as grain size and dendrite arm space and on mechanical properties of AZ91 alloy have been studied [10]. However, quantitative information of β phase is still lacking. Furthermore, the amount and distribution of β phase strongly influence the corrosion resistance of AZ91 alloy [11–13], which is itself also an important consideration for selecting the alloy. β phase may serve as a galvanic cathode and accelerates the corrosion process of α phase matrix if $f_\beta$ is small; but for a high $f_\beta$ β phase may act as an anodic barrier to inhibit the overall corrosion of the alloy [14]. Thus, quantitative information on β phase is valuable.

During the casting of AZ91 alloy, there is a further phase transformation process after solidification—discontinuous precipitation forming lamellas of β phase ($\beta_{\text{-d}}$). This discontinuous precipitation normally initiates at the dendrite/eutectic boundaries, and the precipitates grow towards the interior of α phase grains. $\beta_{\text{-d}}$ lamellas are fine and expected to have a less detrimental effect on mechanical properties of the castings. There has been no specific research conducted regarding the effect of the amount of $\beta_{\text{-d}}$ on corrosion. Thermal conditions affecting discontinuous precipitation in AZ91 alloy after the alloy being solution treated have recently been investigated [15]. But it must be noted that the fraction of $\beta_{\text{-d}}$ in cast

* Corresponding author.
*E-mail address:* tzhu004@aucklanduni.ac.nz (T. Zhu).

0925-8388/$ – see front matter © 2010 Elsevier B.V. All rights reserved.
doi:10.1016/j.jallcom.2010.04.090

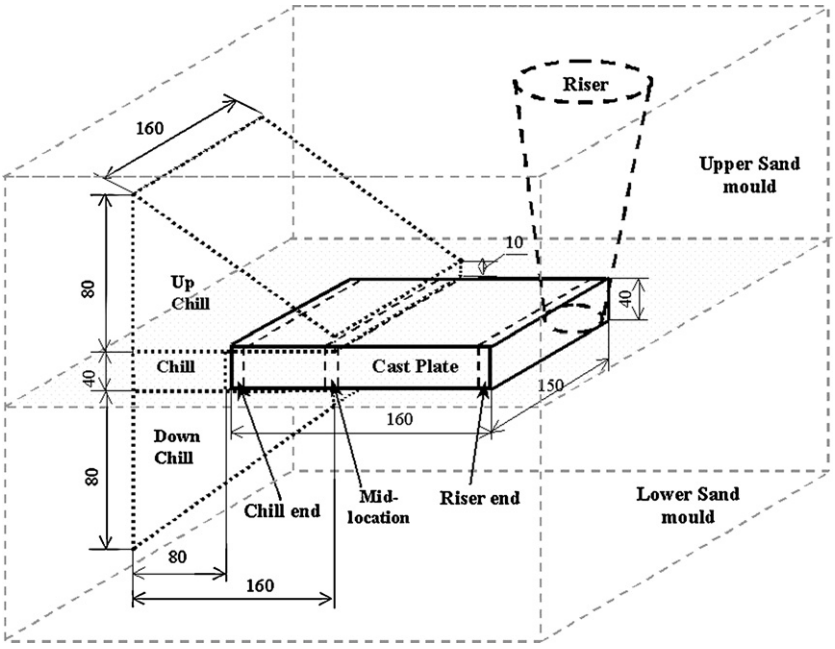


**Fig. 1.** Sand mould, mould cavity and the chill used in the present experiment.

**Table 1**
The nominated chemical composition of AZ91D cast alloy.

| Element | Al | Zn | Mn | Si | Fe | Cu | Ni | Mg |
|---|---|---|---|---|---|---|---|---|
| wt.% | 8.5–9.5 | 0.45–0.96 | 0.17–0.40 | <0.05 | <0.004 | <0.025 | <0.001 | balance |

state has not been determined; and how this fraction is affected by casting conditions has not been studied.

In the present study, AZ91 alloy was cast with various cooling conditions depending on location of the casting. This was achieved by using a sand mould with a chill, which has been used a number of times to study the effect of cooling condition on cast microstructure [10,16,17]. Quantitative analysis on β phase was then conducted using electron backscatter diffraction (EBSD) and image analysis on optical micrographs. The measured values were compared with the predicted values at solidification temperature, and the effect of cooling conditions during casting on the amount of β (both $\beta_{\text{-eut}}$ and $\beta_{\text{-d}}$) phase is discussed.

## 2. Experimental procedures

A cast plate was made with a sand mould, as schematically shown in Fig. 1. The mould was embedded with iron chills at one end of the cast cavity. Commercial ingots of AZ91D, with nominal composition listed in Table 1, were melted and poured into the mould. After casting, the cast plate was sampled in the riser end, middle and chill end locations (as indicated in Fig. 1). Sampling was conducted by sectioning perpendicularly to the solidification direction, and the samples have a dimension of 150 mm × 40 mm × 7 mm.

For a multi phase microstructure, EBSD mapping can be used to accurately determine the fraction of the phases. This is achieved by counting the scanning points on the representative area of the specimen. Fig. 2 shows the morphology of discontinuous β lamellas in the vicinity of $\beta_{\text{-eut}}$ particle. The β lamellas with thickness of ~1 μm can be counted during EBSD mapping with a high resolution, 50–150 nm [18]. Therefore, EBSD mapping provides a total $f_\beta$ which is equal to $f_{\beta\text{-eut}} + f_{\beta\text{-}d}$.

Specimens for EBSD mapping were polished to 1 μm stage following a standard procedure. During the next step the mechanically polished specimen was electrolytically polished in a quiescent bath for ~30 s under a voltage of 1.5 V and current of 5–10 mA. The electrolyte comprises of three parts of 85% phosphoric acid and five parts of ethanol. The specimen was removed from the electrolyte while the current was still on, and rinsed immediately by rapidly running alcohol to minimize the etching effect by the acid.

EBSD mapping was conducted on selected areas of a freshly polished sample at a scanning step of 0.3 μm and a speed of 6 points/s. In order to achieve reliable $f_\beta$ values, a relatively large mapping area of ~300 μm × 300 μm was selected for riser end cast sample with a coarse grain structure and a half of that mapping area was used for the chill end sample with a finer micostructure. A slight oxidation on the sample surface is inevitable even on the freshly polished sample. However, the oxidation generally took place on α phase, and β phase is relatively inert and remains unaffected. Thus, the measured $f_\beta$ values are reliable. The values of confidence index (CI) of EBSD mapping were checked. The values of CI are mostly over 0.2, and minimum is about 0.1. These CI values also suggest the reliable detection of phases in the samples by EBSD method.

Using EBSD analysis, the value of total $f_\beta$ ($=f_{\beta\text{-eut}} + f_{\beta\text{-}d}$) was obtained. As was already explained, it is important to gain quantitative information on $\beta_{\text{-eut}}$ phase in AZ91 cast alloy, which influences significantly its mechanical properties and corrosion resistance. To gain this knowledge, image processing method employing "ImageJ" software was used to quantify $\beta_{\text{-eut}}$. Lamellas of $\beta_{\text{-d}}$ were erased manually from metallographs before the quantitative analysis using "ImageJ". The gray digital micrograph with a sufficient contrast between $\beta_{\text{-eut}}$ phase and the matrix was

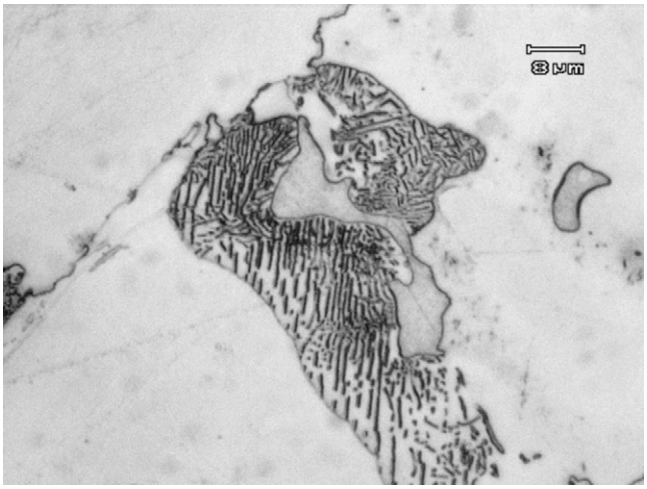


**Fig. 2.** Laminar β phase particles present in the sample taken in the riser end location of the casting.

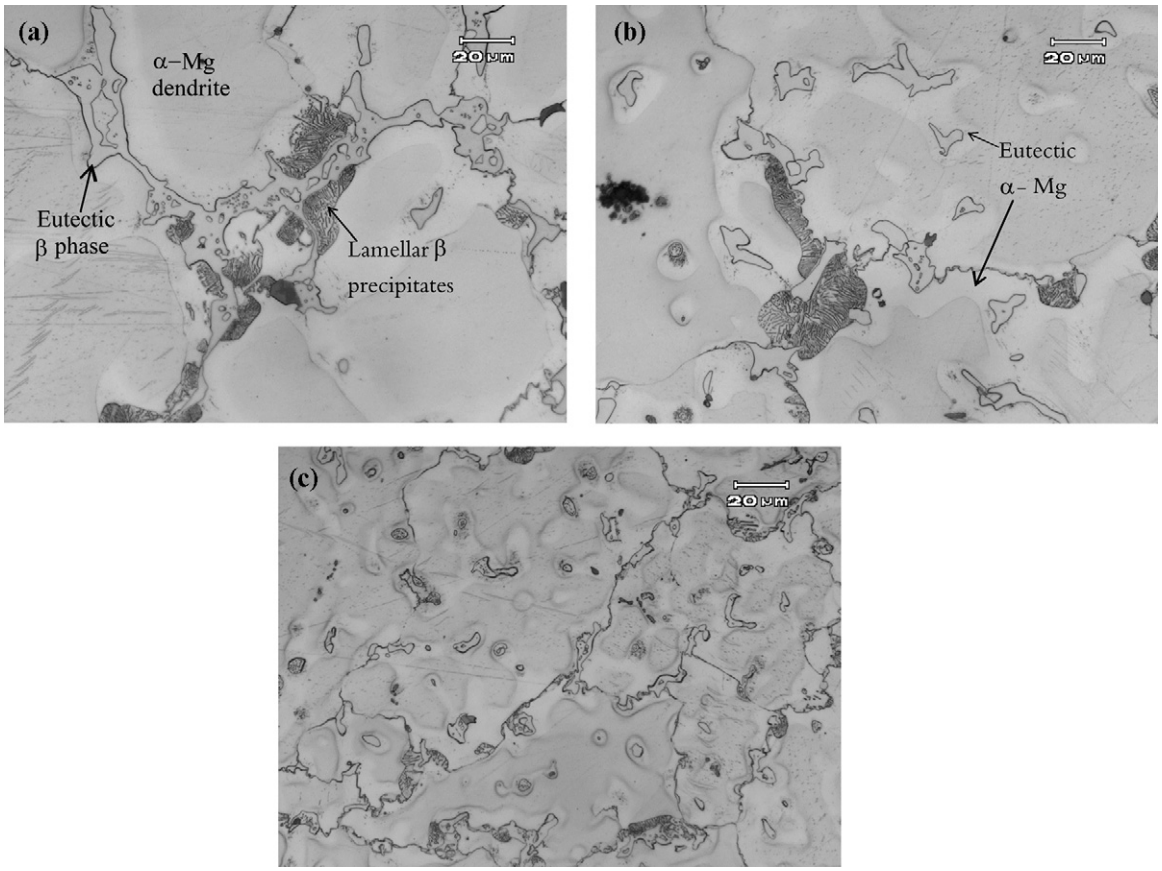


**Fig. 3.** Micrographs taken in (a) riser end, (b) mid-location and (c) chill end samples.

converted into a binary image by applying a threshold. Then, $f_{\beta\text{-}eut}$ was measured on the binary digital image.

Samples for "ImageJ" analysis were polished to 1 μm stage, and etched using "phospho-picral" (0.7 ml $H_3PO_4$, 4–6 g picric acid, and 100 ml ethanol) etchant. The α phase matrix is darkened after etching, leaving the high Al content β phase white. Three digital micrographs were taken for each sample; and each micrograph contained at least 20 grains ensuring reliable measurement of $f_{\beta\text{-}eut}$. To minimise random error, identical conditions were used consistently during sample preparation, capturing and processing of digital microimages.

## 3. Results and discussion

Fig. 3 shows the cast microstructures of samples sectioned at the three specific locations (as indicated in Fig. 1). The $\beta_{\text{-eut}}$ particles in the riser end sample exhibited a partially divorced morphology with α phase islands inside. $\beta_{\text{-eut}}$ particles appeared in the mid-location and chill end samples are more divorced. The particles are highly irregular in the interdendritic regions and more spherical in secondary dendrite arm spaces. Towards the chill end, the dendrites are smaller and interdendritic areas are larger, and hence the $\beta_{\text{-eut}}$ particles became more discrete and most $\beta_{\text{-eut}}$ particles (with smaller size) were trapped within the dendrite arms in a single dendrite. These features are in agreement with literature [2,19,20]. Lamellas of $\beta_{\text{-d}}$ are a clear feature of β phase and present in all three locations of the casting.

During tensile testing, the initial microcracks were observed inside the β phase particles, as shown in Fig. 4a, when the sample was tested to a very low strain level (less than 2%). This indicates the brittle nature of the intermetallic β phase. Fig. 4b shows an example of the intergranular fracture in a mid-location tensile sample. A large amount of brittle β phase particles along the grain boundaries favor the coalescence and the propagation of microcracks. The alloy could not withstand a significant amount of elongation, and fractured at a low strain level. Hence, the AZ91 cast alloy generally exhibits poor ductility. This is in agreement with the results from Cao and Wessén [9].

EBSD quantitative analyses were conducted on the riser end and the chill end samples, representing the two extreme cases of cooling condition. Fig. 5 shows an EBSD orientation map (Fig. 5a), and the phase image (Fig. 5b) on a selected scanning area of a riser end sample. Quantitative results are summarized in Table 2. Two factors may affect the accuracy slightly. Firstly, there was no diffraction solution at certain points due to the shadow effect at α/β interfaces. The percentage of good diffraction points (showing clear diffraction patterns) for the chill end sample was slightly lower than that for the riser end sample, as shown in Table 2. This was due to the small size of $\beta_{\text{-eut}}$ particles and thus the resultant larger area of α/β interfaces. In general, however, the percentage (97–98%) of good diffraction points can be regarded high. The second factor relates to the minor inclusions ($Mg_2Si$, $Al_8Mn_5$, etc.). However, their amounts are very low and not expected to affect the EBSD analytical outcome significantly.

The average $f_\beta$ values, being 11.2% and 12.3%, for the riser end and chill end samples, respectively, agree well with the results reported recently by Yakubtsov et al. [4] on an AZ80 cast alloy to be 10.2% for non-grain refined and 11.8% for grain refined cast samples. Their measurements were based on quantitative metallography using SEM images. Our values and those from Yakubtsov et al. [4] both show a slight higher $f_\beta$ with a finer microstructure. A slightly overall higher $f_\beta$ in our case is due to ~1% higher Al content in AZ91 cast alloy than that in AZ80 alloy used by Yakubtsov et al. [4].

The measured values of $f_{\beta\text{-}eut}$ using 'ImageJ' are presented in Fig. 6. The measurements were conducted on all micrographs with the same magnification. Therefore, the measured $f_{\beta\text{-}eut}$ in the riser

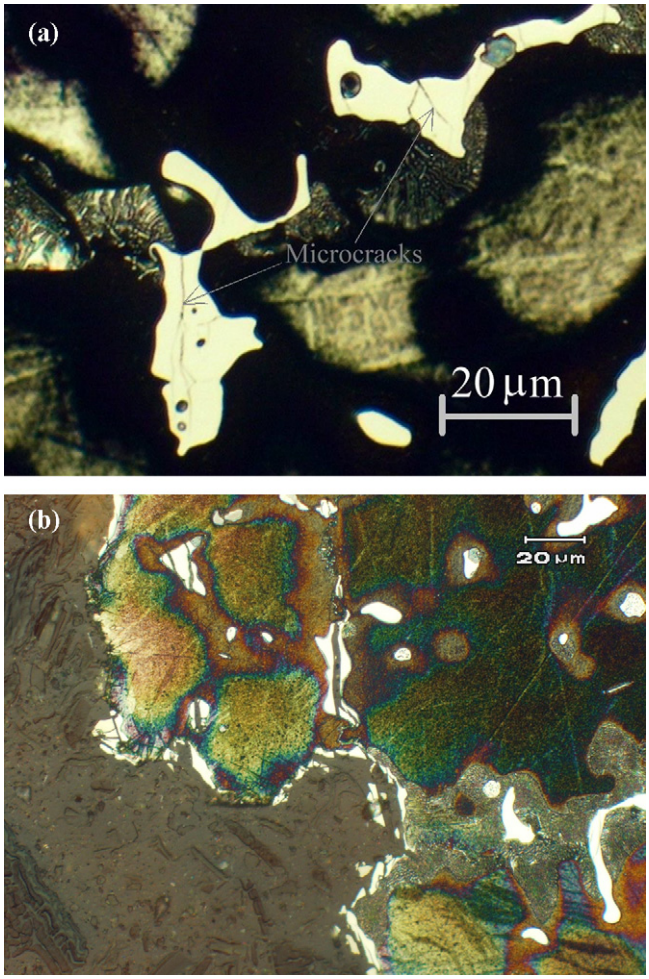


**Fig. 4.** Optical micrographs showing (a) the initial microcracks occurred inside the β phase particles at a very low strain level (<2%) (horizontal tensile load direction), and (b) intergranular fracture of a mid-location tensile sample fractured at a strain of 2.6% (25 mm gauge length).

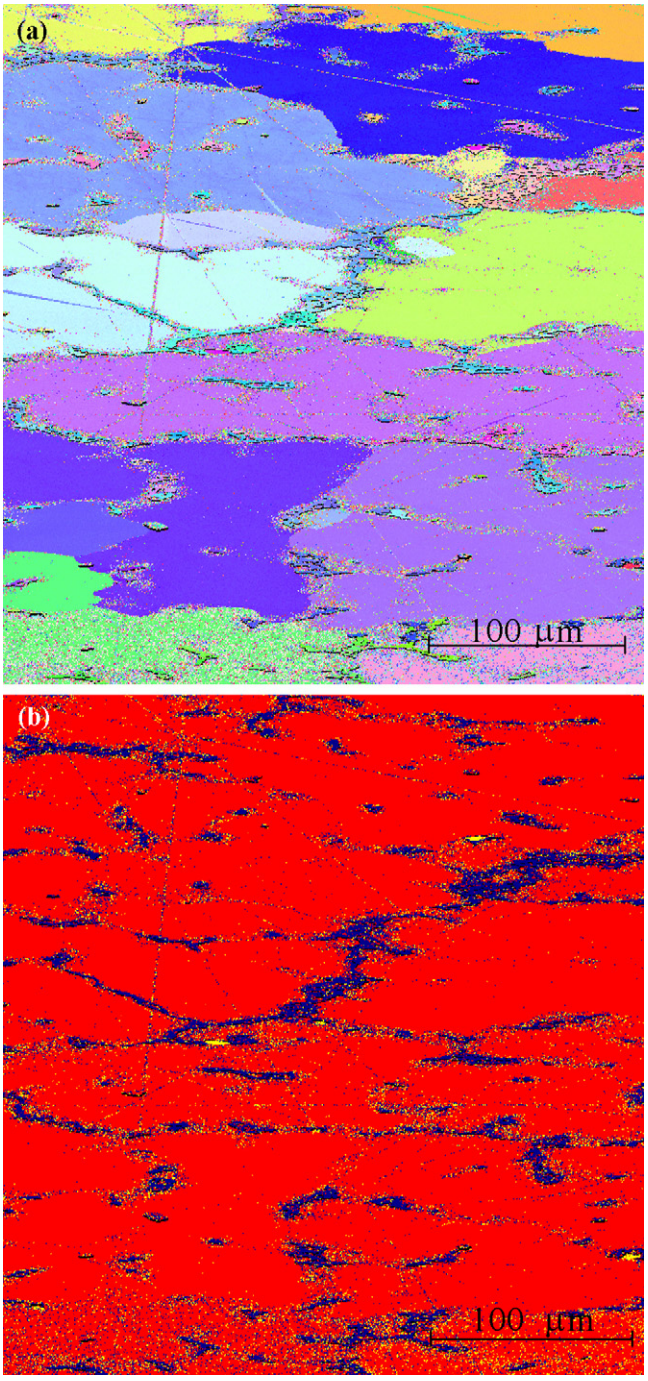


**Fig. 5.** EBSD (a) orientation map, and (b) phase image taken on a selected scanning area of a riser end sample.

end sample shows a larger standard error due to the less even distribution of $\beta_{\text{-eut}}$ particles in this larger grained sample. Two important features which the "ImageJ" measurements, together with EBSD measurements, have shown are clear. The first is that $f_{\beta\text{-}eut}$ (7.8, 5.7 and 4.7 vol.% in riser end, mid and chill end locations, respectively) decreases towards the chill end. The second is that $f_{\beta\text{-}eut}$ is significantly lower than $f_{\beta}$ (11–12 vol.%). These two features also mean that a significant amount of lamellar $\beta_{\text{-d}}$ phase formed during cooling after solidification; and a higher amount of this $\beta_{\text{-d}}$ phase formed towards the chill end. Explanation on these features of $\beta_{\text{-eut}}$ and $\beta_{\text{-d}}$, based on solidification theory and Mg–Al phase relation, together with the casting condition, is given below.

In order to understand the different values of $f_{\beta}$, $f_{eut\text{-}\beta}$ and $f_{\beta\text{-}d}$ as described above, it is helpful to first briefly consider the system thermodynamically in equilibrium (not realistic), before a detailed consideration is given to the non-equilibrium solidification process (realistic). If the cooling during casting was infinitely slow, equilibrium fraction of β phase ($f_{equ\text{-}\beta}$) can be predicted using the known phase diagram. For this, it is important to consider two fractions, which can be approximated according to the Mg–Al binary phase diagram. The first is $f_{equ\text{-}\beta} = 0$ at $T_E$, meaning that there is no β phase when temperature decreases to $T_E$ (complete solidification). The second is $f_{equ\text{-}\beta} = 17$ vol.% at room temperature. The values of $f_{equ\text{-}\beta}$ as a function of temperature is given in Fig. 7, which are calculated based on the equilibrium maximum soluble content of Al in Mg and the composition of β phase obtained from the Mg–Al binary phase diagram, and taking densities of α phase 1.8 g/cm$^3$ and β phase 2.1 g/cm$^3$.

**Table 2**
The average fractions of β phase in two cast samples measured by EBSD mapping.

| | Riser end | Chill end |
|---|---|---|
| Fraction of α-Mg, % | 82.5 | 80 |
| Fraction of Mg oxide, % | 4.0 | 4.8 |
| % of good points | 97.7 | 97.1 |
| Fraction of β phase, % | 11.2 | 12.3 |

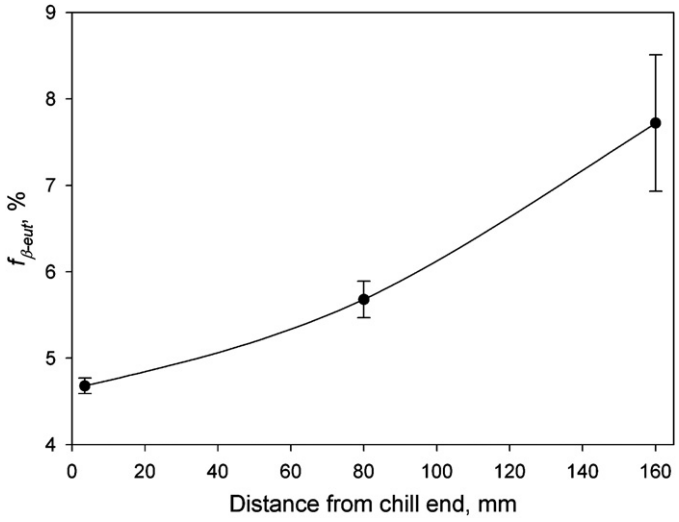


**Fig. 6.** $f_{\beta\text{-}eut}$ (with standard errors) measured using "Image J" on the three location specific samples.

Under non-equilibrium cooling, as is the case of most if not all casting processes, $f_\beta \gg 0$ at $T_E$. The value of $f_\beta$ (in vol.%) can be approximately estimated using the well known Scheil equation [21] of solidification:

$$f_E = \left(\frac{C_E}{C_0}\right)^{1/(k-1)} \quad (1)$$

where $f_E$ is the weight fraction of eutectic, $C_E$ is the eutectic composition (=33.3 wt.% Al), $C_0$ is the alloy composition (=9 wt.% Al), $k$ is the partition ratio (≈0.378), the lever rule:

$$f_{\beta\text{-}wt\%} = \frac{C_E - C_\alpha}{C_\beta - C_\alpha} \cdot f_E \quad (2)$$

where $f_{\beta\text{-}wt.\%}$ is the weight fraction of β phase, $C_\alpha$ and $C_\beta$ are compositions of α phase (=12.6 wt.% Al) and β phase (=41.5 wt.% Al), respectively, and also:

$$f_\beta = \frac{\rho_\alpha f_{\beta\text{-}wt\%}}{\rho_\beta - f_{\beta\text{-}wt\%}(\rho_\beta - \rho_\alpha)} \quad (3)$$

where $f_\beta$ is the volume fraction of β phase, $\rho_\alpha$ is the density of α phase (≈1.8 g/cm$^2$) and $\rho_\beta$ is the density of β phase (≈2.1 g/cm$^2$). The value of $f_\beta$ is thus estimated, using equations (1) to (3), to be ~8.6 vol.% immediately after solidification at $T_E$ (at ~426 °C for AZ91 cast alloy [22,23] which is lower than the binary equilibrium $T_E$ at 437 °C).

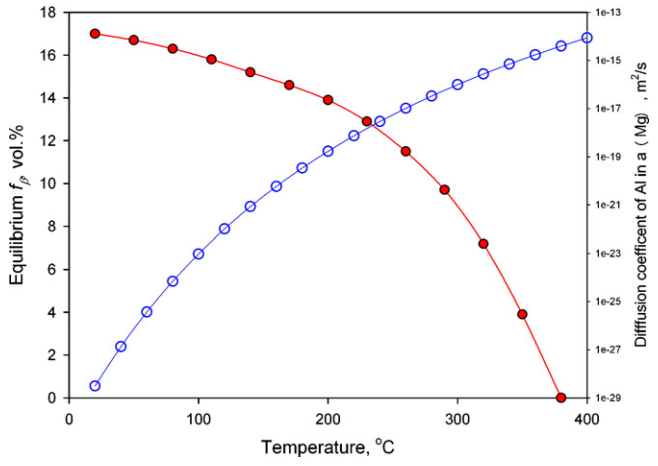


**Fig. 7.** Approximate equilibrium $f_\beta$ and diffusion coefficient of Al in α(Mg) as a function of temperature.

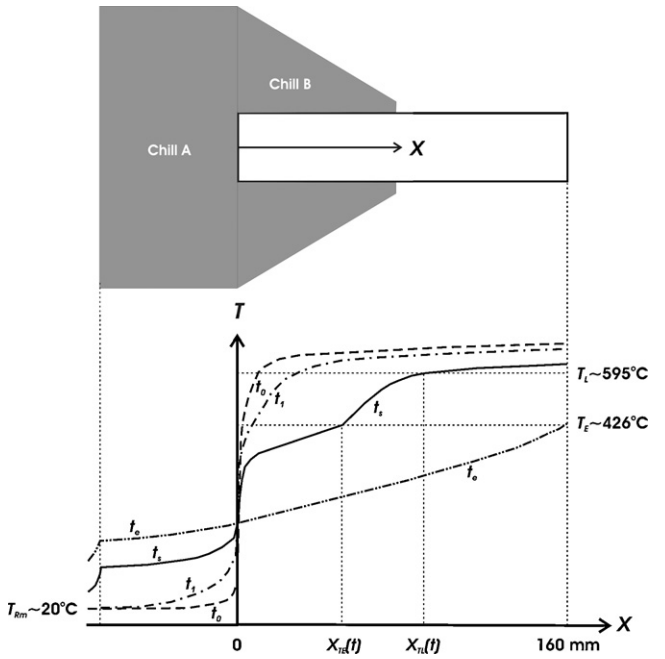


**Fig. 8.** Schematics of the casting plate and chill and of the corresponding temperature profiles at various times: $t_0$ means the time immediately after pouring, $t_1$ represents an early stage and $t_s$ any stage of solidification and finally $t_e$ means the time of complete solidification. $T_L$ and $T_E$ represent the liquidus and eutectic temperatures, respectively, and $X_{TE}(t)$–$X_{TL}(t)$ represents the size of the mushy zone at $t$.

The use of Scheil equation overestimates $f_{\beta\text{-}eut}$ as it does not take into account the back diffusion and the solute build-up in front of the solid–liquid interface during solidification. Thus the predicted value is slightly higher than the measured values in the riser end sample shown in Fig. 6. The degree of back diffusion is however lower and $f_{\beta\text{-}eut}$ due to the non-equilibrium solidification is likely to be higher for a higher cooling rate. Thus the significantly lower measured $f_{\beta\text{-}eut}$ values when compared to the predicted values towards the chill end (Fig. 6) is unlikely to be due to the assumptions used in Scheil equation. Rather, $f_{\beta\text{-}eut}$ in the chill end sample should be expected to be at least equal to, if not higher than, that in the riser end sample immediately after solidification. If the casting was maintained at close to $T_E$, the ~8 vol.% β phase dissolved, moving towards the equilibrium state. The complete dissolution takes a number of hours and is the reason why 16–24 h treatment at 413–418 °C to dissolve β-phase is recommended [24]. For the casting in the present case, as it was likely to only stay at temperatures of above 400 °C for seconds/minutes, $f_{\beta\text{-}eut}$ may not reduce to a very low value.

Various locations of the casting are now considered. For a discussion purpose, temperature profiles of the casting and the chill at various times may be suggested, as illustrated schematically in Fig. 8. The features regarding the cooling condition during solidification along the casting are based on measured values obtained from experiments using the same alloy and a similar mould from Cáceres et al. [10]. Their data show that at ~20 mm from the chill end solidification time was 20 s and the time was over 200 s in locations near the riser end. The same mould was also used for Al–Si–Mg cast alloy [17]. The measured values of the mean cooling rates from the liquidus to the eutectic temperature varied from a maximum of 6 °C/s some 15 mm from the chill end to 0.2 °C/s at the riser end of the plate. Fig. 8 reflects this that in the initial stages ($t_0$, $t_1$) of solidification (solidification near the chill), temperature gradient is

high, chill temperature is low, and thus solidification time should be short. In a later stage ($t_s$), chill temperature has increased and heat conducted away slowly, and thus temperature gradient is low and solidification time becomes long.

Heat is primarily extracted to the chill during the initial solidification. This can be indicated by considering that the thermal diffusivity of the chill material is about 17 times higher than sand. As time increases the temperature of the chill increases. An approximation, by assuming that the chill extracted all the super heat and latent heat, indicates that the average chill temperature can increase to ~180 °C. The heating of the chill results in the diminishing chilling effect. This means that the cooling rate and thus the solidification rate decreases as solidification proceeds from the chill end to the riser end, as shown by the measured data from Cáceres et al. [10] and reflected also in Fig. 8.

Further to the heating of chill, due to the existence of an air gap and thus a temperature difference at the casting–chill interface, the rate of heat transfer to the chill should reduce significantly after the initial solidification. On the other hand, heat from the rest of the casting keeps flowing through the chill end of the casting to the chill. Thus, it should be reasonable to assume that the chill end of the casting remains at a high temperature for a longer period.

During the initial period of solidification where the chill end of the casting has solidified but remains at high temperatures, some dissolution of $\beta_{\text{-eut}}$ is expected. This may explain the measured $f_{\beta\text{-}eut}$ is low and significantly lower than the value predicted using the Scheil equation in the chill end location. On the other hand, in the riser end location once the solidification is completed temperature can reduce more rapidly as no further additional heat flows into the location. Thus the solidified riser end of the casting does not remain at a high temperature after solidification for dissolution of $\beta_{\text{-eut}}$. This explains that at riser end location, the measured $f_{\beta\text{-}eut}$ of 7.8 vol.% is higher and closer to the estimated value of 8.6 vol.% using Scheil equation.

As has been indicated, the chill could reach the temperature of 180 °C and thus it is reasonable to assume that after complete solidification of the entire casting, the casting can be expected to remain at 200–250 °C for an extended period of time. When the casting remains at 200–250 °C, as shown in Fig. 7, if $f_\beta$ is not yet 11–12 vol.% $f_{\beta\text{-d}}$ needs to increase through precipitation from α-Mg phase with supersaturated Al. A measured value of 11–12 vol.% in our case and 10–11 vol.% in Yakubtsov et al.'s case [4] suggests that at that temperature range short range diffusion required for the discontinuous precipitation is sufficient. Although $f_\beta$ should continue to increase during subsequent cooling, the increasing difficulty due to the dramatic reduction in diffusion rate as temperature decreases, as is also plotted in Fig. 7, may prevent a significant further precipitation of β phase. To illustrate, given a same concentration gradient and for a same amount of diffusion flux, the time it takes at 200 °C is ~50 times longer than that at 250 °C. Thus, the further increase in $f_\beta$ becomes increasingly difficult as temperature decreases.

## 4. Conclusions

The cooling rate during casting affects $f_{\beta\text{-}eut}$ and $f_{\beta\text{-}d}$ significantly. In the location subjected initially to chilling, a significant amount of $\beta_{\text{-eut}}$ phase dissolved and a high amount of $\beta_{\text{-d}}$ precipitates formed due to the longest period at high temperature after solidification. The amount of $\beta_{\text{-eut}}$ phase dissolution was lower towards riser end location, likely the result of remaining at the very high temperature only for a short period of time after solidification in that location. The total amount of β phase, which was 11–12 vol.% and was the sum of the two (amounts of $\beta_{\text{-eut}}$ and $\beta_{\text{-d}}$), was however not affected by location significantly. This can be explained by the chilling effect of the heated chill diminished after the complete solidification of the casting. Thus the whole casting remained at elevated temperatures for a sufficiently long period of time allowing $f_{\beta\text{-}d}$ thus $f_\beta$ to increase toward the equilibrium value. This increase of $f_\beta$ must have later practically stopped when diffusion became the severe limiting factor as temperature continued to decrease.

## References

[1] S. Barbagallo, H.I. Laukli, O. Lohne, E. Cerri, J. Alloys Compd. 378 (2004) 226.
[2] M.D. Nave, A.K. Dahle, D.H. StJohn, Magnesium Technology 2000, Proceeding of TMS Annual Meeting, Nashville, USA, 2000.
[3] M.S. Dargusch, M. Nave, S.D. McDonald, D.H. StJohn, J. Alloys Compd. 492 (2010) L64.
[4] I.A. Yakubtsov, B.J. Diak, C.A. Sager, B. Bhattacharya, W.D. MacDonald, M. Niewczas, Mater. Sci. Eng. A 496 (2008) 247.
[5] L.A. Dobrzanski, T. Tanski, L. Cízek, Z. Brytan, J. Mater. Process. Technol. 192–193 (2007) 567.
[6] S. Kleiner, O. Beffort, A. Wahlen, P.J. Uggowitzer, J. Light Met. 2 (2002) 277.
[7] Y.Z. Lü, Q.D. Wang, W.J. Ding, X.Q. Zeng, Y.P. Zhu, Mater. Lett. 44 (2000) 265.
[8] A. Srinivasan, J. Swaminathan, M.K. Gunjan, U.T.S. Pillai, B.C. Pai, Mater. Sci. Eng. A 527 (2010) 1395.
[9] H. Cao, M. Wessén, Metall. Mater. Trans. A 35 (2004) 309.
[10] C.H. Cáceres, C.J. Davidson, J.R. Griffiths, C.L. Newton, Mater. Sci. Eng. A 325 (2002) 344.
[11] L. Wang, B.P. Zhang, T. Shinohara, Mater. Des. 31 (2010) 857.
[12] Z. Wen, C. Wu, C. Dai, F. Yang, J. Alloys Compd. 488 (2009) 392.
[13] A.D. Südholz, N. Birbilis, C.J. Bettles, M.A. Gibson, J. Alloys Compd. 471 (2009) 109.
[14] G. Song, A. Atrens, M. Dargusch, Corros. Sci. 41 (1998) 249.
[15] K.N. Braszczynska-Malik, J. Alloys Compd. 477 (2009) 870.
[16] C.H. Cáceres, C. Davidson, J.R. Griffiths, Q. Wang, Metall. Mater. Trans. A 30 (1999) 2611.
[17] C.H. Cáceres, C. Davidson, J.R. Griffiths, Mater. Sci. Eng. A 197 (1995) 171.
[18] F.J. Humphreys, J. Microsc. 195 (1999) 170.
[19] A.K. Dahle, Y.C. Lee, M.D. Nave, P.L. Schaffer, D.H. StJohn, J. Light Met. 1 (2001) 61.
[20] M.D. Nave, A.K. Dahle, D.H. StJohn, Int. J. Cast Met. Res. 13 (2000) 1.
[21] W. Kurz, D.J. Fisher, Fundamentals of Solidification, third ed., Trans Tech, Aedermannsdorf, 1989.
[22] T.P. Zhu, Z.W. Chen, W. Gao, Mater. Sci. Eng. A 416 (2006) 246.
[23] Y. Wang, B. Sun, Q. Wang, Y. Zhu, W. Ding, Mater. Lett. 53 (2002) 35.
[24] M.M. Avedesian, H. Baker, Magnesium and Magnesium Alloys, ASM International, 1999.